Volume 27
Number 10
14 March 2025
Pages 4979–5406

PCCP

Physical Chemistry Chemical Physics

rsc.li/pccp

25 YEARS ANNIVERSARY

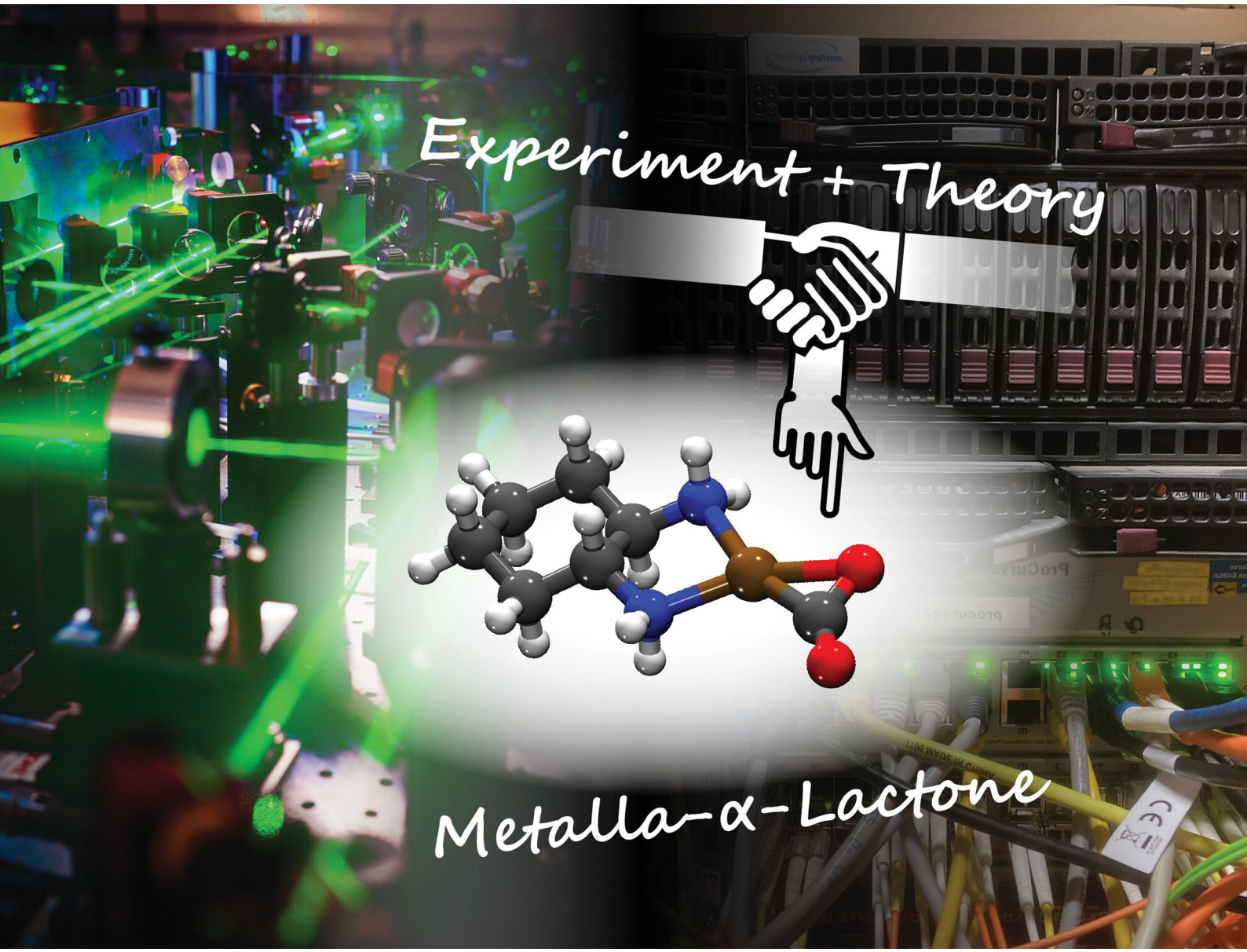

ISSN 1463-9076

ROYAL SOCIETY OF CHEMISTRY

PAPER

Peter Vöhringer *et al.*

Photoinduced formation of a platina-α-lactone – a carbon dioxide complex of platinum. Insights from femtosecond mid-infrared spectroscopy

PCCP Owner Societies

PCCP

ROYAL SOCIETY OF CHEMISTRY

PAPER

View Article Online
View Journal | View Issue

Cite this: *Phys. Chem. Chem. Phys.*, 2025, **27**, 5012

Photoinduced formation of a platina-α-lactone – a carbon dioxide complex of platinum. Insights from femtosecond mid-infrared spectroscopy†

Markus Bauer, ‡ Raphaela Post,‡ Luis I. Domenianni and Peter Vöhringer *

Received 6th October 2024,
Accepted 12th January 2025

DOI: 10.1039/d4cp03840a

rsc.li/pccp

The binding of carbon dioxide to a transition metal is a complex phenomenon that involves a major redistribution of electron density between the metal center and the triatomic ligand. The chemical reduction of the ligand reveals itself unambiguously by an angular distortion of the CO_2-molecule as a result of the occupation of an anti-bonding π-orbital and a shift of its antisymmetric stretching vibration, ν_3, to lower wavenumbers. Here, we generate a carbon dioxide complex of the heavier group-10 metal, platinum, by ultrafast electronic excitation and cleavage of CO_2 from the photolabile oxalate precursor, oxaliplatin, and monitored the ensuing primary dynamics with ultrafast mid-infrared spectroscopy. A neutral and thermally relaxed CO_2-molecule is detected in the ν_3-region within 60 ps after impulsive excitation with 266 nm light. Concurrently, an induced absorption peaking at 1717 cm^{-1} is observed, which is distinctly up-shifted relative to the oxalate stretching bands of the precursor and which resembles the C=O stretching absorption of organic ketones. Accompanying density functional theory suggests that the 1717 cm^{-1}-absorption arises from a Pt–CO_2 product complex featuring a side-on binding mode, which can indeed be regarded as a ketone; specifically, as the metalla-α-lactone, 1-oxa-3-platinacyclopropan-2-one.

Introduction

Exploiting, on an industrial scale, carbon dioxide as an entry material for fine chemicals is a compelling strategy for reducing the man-made carbon footprint and ultimately adhering to international climate protocols.[1–9] A primary obstacle in developing CO_2-based added value chains lies in the thermodynamic stability of carbon dioxide (standard free enthalpy of formation at 298.25 K, ΔG_f^θ = −393.51 kJ mol^{-1}),[10] which inevitably demands some form of energy supply for any chemical transformation that seeks to lower the oxidation state at the central C-atom, *e.g.* in fuels.[11,12] However, to generate high caloric compounds from CO_2 (*e.g.* methane, methanol, formaldehyde, formic acid, and CO), the energy supply must bypass a dissipative heat transfer for reasons of ecological and societal sustainability. Thus, a variety of electrochemical,[13–15] photochemical,[16–19] biochemical[20–23] as well as homogeneous[24–28] and heterogeneous[29–32] chemical-catalytic schemes of carbon dioxide activation are currently being pursued with high priority.

Here, we wish to contribute to the field of transition-metal (TM) mediated CO_2-activation.[33–39] A TM-center with formal oxidation state, Q, can serve as an electron reservoir for a redox non-innocent ligand. Following this notion, CO_2 can bind either as a neutral

$$M^Q + CO_2 \rightarrow M^Q - CO_2 \quad (1)$$

or as a radical anion

$$M^Q + CO_2 \rightarrow M^{Q+1} - CO_2^{\bullet -} \quad (2)$$

or as a closed–shell dianion

$$M^Q + CO_2 \rightarrow M^{Q+2} - CO_2^{2-}. \quad (3)$$

Only in the first case is the metal's oxidation state preserved and the original non-activated form of the carbonaceous ligand retained. This form of binding is reminiscent of a physisorptive state of CO_2 on a flat metal surface with negligible perturbation of the electronic and molecular structure of the triatomic moiety.[40]

However, a metal-to-ligand one-electron transfer generates the carbon dioxide radical anion, $CO_2^{\bullet -}$,[41] as emphasized in reaction (2). Such a reductive activation occupies a low-lying

Abteilung für Molekulare Physikalische Chemie, Clausius-Institut für Physikalische und Theoretische Chemie, Rheinische Friedrich-Wilhelms-Universität Bonn, Wegelerstraße 12, 53115 Bonn, Germany. E-mail: p.voehringer@uni-bonn.de

† Electronic supplementary information (ESI) available. See DOI: https://doi.org/10.1039/d4cp03840a

‡ These authors contributed equally to this work. Shared first authors.

anti-bonding π*-orbital of the heterocumulene and results in the typical angular distortion as predicted by Walsh's rules.[42] Two binding modes of the bent radical anion have been observed experimentally; namely, the $\eta^{(1)}_{C}$-mode with σ-bonding between the TM-center and the ligand's central carbon atom, and the $\eta^{(1)}_{O}$-mode featuring a σ-bond between the TM and one of the ligand's terminal oxygen atom.[34,35,38,43,44]

As expressed by reaction (3) a metal-to-ligand two-electron transfer generates the doubly negatively charged carbonite, CO_2^{2-}; a bent dianion,[45] which prefers a side-on coordination by forming both, TM–O and TM–C σ-bonds.[35] In analogy to the Dewar–Chatt–Duncanson model, the dihaptic side-on mode can also emerge from dative binding of the neutral heterocumulene *via* π-donation to the TM's d-orbitals. Therefore, an adequate quantum-mechanical description of the electronic structure associated with the $\eta^{(2)}_{C,O}$-mode may require a mixed wavefunction accounting for both configurations (1) and (3) simultaneously.[46]

The species, $[Ni(CO_2)(PCy_3)_2]$, with Cy = cyclohexyl, was discovered by Aresta and coworkers[47,48] already half a century ago and represents the very first mononuclear TM–CO_2 complex that was isolated and fully characterized. Both, in crystalline form and in liquid solution, the complex displays the $\eta^{(2)}_{C,O}$ side-on structure but evidence was obtained from nuclear magnetic resonance (NMR) and Fourier-transform infrared (FTIR) spectroscopy that the species can also pass through a $\eta^{(1)}_{O}$ end-on intermediate involved in the internal Ni–CO_2 rotation.[44]

In the recent past, we have used the photoinduced decarboxylation reaction of TM-oxalates to access TM–CO_2 complexes according to[43,49,50]

$$M^{Q}(C_2O_4^{2-}) + h\nu \rightarrow M^{Q-2/Q-1/Q}(CO_2^{0/\bullet-/2-}) + CO_2. \quad (4)$$

Here, the dianionic oxalate ligand, $C_2O_4^{2-}$, is heterolytically cleaved by releasing a neutral CO_2-molecule and leaving behind a carbon dioxide ligand attached to the metal center. In principle, the emerging TM–CO_2 product can adopt any of the three configurations (1)–(3).

A variety of factors will ultimately govern the electronic structure of the product.[43,49,50] The CO_2-loss entails the cleavage of the oxalate's C–C-bond in addition to the rupture of one of the M–O bonds. These bond breakages eliminate a closed–shell triatomic fragment and hence, the spin of the parent oxalate must be preserved during the formation of the primary TM–CO_2 product. However, the decarboxylation is induced upon absorption of a photon and it may thus very well be that the CO_2-elimination is facilitated by a preceding non-adiabatic transition of the optically prepared, electronically excited state; *i.e.*, by an internal conversion or an intersystem crossing.

We have recently explored the photo-decarboxylation dynamics with formation of TM–CO_2 complexes using two distinct d^5-iron(III) oxalate model systems; namely, trisoxalatoferrate(III) ($[Fe^{III}(C_2O_4)_3]^{3-}$, or ferrioxalate)[43,51] and (1,4,8,11-tetraazacyclotetradecane)oxalatoiron(III) ($[Fe^{III}(cyclam)(C_2O_4)]^{+}$).[49,50] Both systems occupy a high-spin (S = 5/2) ground state but upon release of CO_2, the resulting Fe–CO_2 motif is dressed either with weak-field oxalate ligands or strong-field secondary amine ligands. Intriguingly, the primary product, $[(C_2O_4)_2Fe(CO_2)]^{3-}$, of the ferrioxalate photolysis was found to occupy a sextet ground-state featuring the $\eta^{(1)}_{O}$-mode whereas the primary product, $[(cyclam)Fe(CO_2)]^{+}$, of the tetraamine-dressed precursor has a quartet ground-state adopting the $\eta^{(2)}_{C,O}$-mode. These findings suggest that the TM–CO_2 binding mode can actually be controlled through properly designing the ligand field.[49,50]

Here, we wish to access photochemically a CO_2-complex that closely resembles Aresta's complex, $[Ni(CO_2)(PCy_3)_2]$, but containing the heavier group-10 metal, Pt, and having the two alkyl phosphanes replaced by the less floppy and sterically less demanding bidentate ligand, (1*R*,2*R*)-cyclohexanediamine (dach). As a precursor we will use the photolabile complex, [(1*R*,2*R*)-cyclohexanediamine]oxalatoplatinum(II), or oxaliplatin ([**1**]), and elucidate in detail the dynamics of its photoinduced decarboxylation according to Scheme 1. This reaction is then

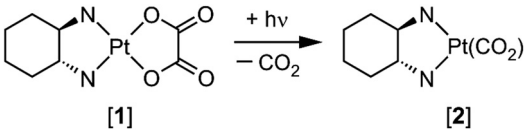

[1] [2]

Scheme 1 Photoinduced decarboxylation of oxaliplatin.

expected to generate our target structure, (carbon dioxide)[(1*R*,2*R*)-cyclohexanediamine]platinum ([**2**]). To this end, we utilize ultraviolet-pump/mid-infrared-probe (UV/MIR) spectroscopy with femtosecond duration laser pulses; a technique, which has proven particularly powerful for exploring the structure and the reactivity of highly elusive transition metal complexes in liquid solution and under ambient conditions.[52]

Methods

Experimental

Oxaliplatin (purity 99.81%) and dimethyl sulfoxide (ACS reagent) was purchased from Molekula Ltd and Sigma Aldrich, respectively, and used without further purification. Electronic absorption spectra were recorded in the ultraviolet-to-visible (UV-Vis) region with a PerkinElmer Lambda 365+ spectrophotometer at a wavelength resolution of 1 nm. Fourier transform (FT) infrared (IR) spectra were collected with a Bruker Vertex 70 Spectrometer at a wavenumber resolution of 0.25 cm^{-1}. UV-pump/IR-probe-spectroscopy was carried out with a home-built spectrometer described in detail elsewhere.[53] In short, a fraction of the fundamental output of a Ti:sapphire oscillator/regenerative amplifier front-end (Newport Spectra Physics, Solstice Ace, pulse duration 60 fs, center wavelength 800 nm) is frequency tripled to generate pump pulses centered at 266 nm. To produce the probe pulses, a second fraction of the same front-end output was used to drive an optical parametric amplifier (TOPAS Prime, Light Conversion) whose signal and idler pulses were frequency-downconverted to the mid-IR-region *via* difference-frequency generation in a type-I $AgGaS_2$-crystal. The probe pulses were subsequently split into detection

and reference pulses of similar intensities. A pump–probe delay was introduced by sending the detection pulses through a motorized linear translation stage. The relative pump–probe polarization was set to the magic angle to suppress signal contributions arising from molecular rotations. Detection and reference pulses were focused into the sample with a Au-coated 90° off-axis parabolic mirror (OAM, 10 cm focal length). After passing through a chopper disc that blocks every other pulse, the UV-pump beam is spatially overlapped inside the sample with the detection pulses at a crossing angle of 5°. The pump waist inside the sample was adjusted to 1 mm using a fused silica with a focal length of 400 mm. Behind the sample, probe and reference beams were collimated with another OAM and independently steered onto the two entrance slits of an imaging spectrometer (Horiba, iHR 320) whose exit plane was equipped with a 2 × 32 pixel HgCdTe-array detector (Infrared associates) thereby enabling a referenced detection of the pump-induced differential absorbance. The sample was circulated with a gear pump through a home-built transmission flow cell comprised of two CaF_2 windows separated by 200 μm with a Pb-spacer.

Computational

Electronic structure calculations were carried out within the framework of density functional theory (DFT) and its time-dependent (TD) variant using the Gaussian 16 program package.[54] TD-DFT calculations were conducted in the Tamm–Dancoff-approximation[55] and the B3LYP functional[56] was used throughout. In addition, Grimme's dispersion correction,[57] D3, with Becke–Johnson (BJ) damping was applied in all calculations. Ahlrich's triple-zeta valence basis, def2-TZVP,[58] was assigned to the Pt-center, all atoms of the oxalate ligand as well as to the two N-atoms. The 60 core electrons of platinum were replaced by the quasi-relativistic pseudopotential, ECP60MWB,[59] of the Stuttgart/Cologne group. Finally, the smaller split-valence basis, def2-SVP, was assigned to all remaining atoms. Solvent effects were accounted for within the conductor-like polarizable continuum model[60] for DMSO. The model chemistry is abbreviated from hereon B3LYP/GenECP. Geometry optimizations were carried out utilizing Gaussian's built-in "Tight" convergence criteria. Relaxed structures were confirmed to be true minima of the respective potential surface by performing a harmonic normal mode analysis with analytical force constants and verifying that all eigenvalues of the Hessian were positive. Excited-state geometry optimizations were carried out analogously except for loosening the convergence criteria by setting Gaussian's internal option IOp (1/7 = 50).

Results and discussion

Stationary spectroscopy

The electronic absorption spectrum of [**1**] in UV-Vis region is depicted in Fig. 1. In DMSO solution, only an absorption onset around 330 nm is detected, which levels off at *ca.* 260 nm. The absorption of the solvent unfortunately prevents a reliable measurement of the spectrum for shorter wavelengths.

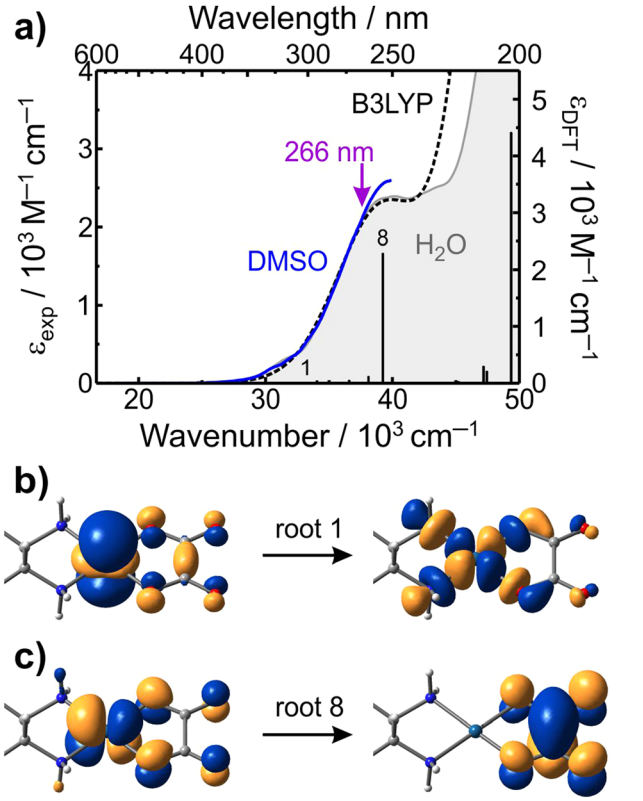

Fig. 1 (a) Experimental UV-Vis absorption spectrum of [**1**] in DMSO (blue curve) and in aqueous solution (gray), both recorded at room temperature. The dashed black curve is the UV-Vis spectrum predicted by TD-B3LYP/GenECP. The associated relative oscillator strengths of the underlying resonances are given by the sticks. The theory predicts an absolute oscillator strength of 0.1041 for the transition to root 8. The pump wavelength of 266 nm used in this study is highlighted by the vertical arrow. (b) Natural transition orbitals associated with the lowest electronic excitation of oxaliplatin at the relaxed geometry of the ground state. (c) Same as in (b) but for the strongest electronic excitation in the near ultraviolet region around 255 nm.

The transmission of water extends much farther into the ultraviolet, which enables the recording of the absorption spectrum of [**1**] in aqueous solution for much shorter wavelengths (*cf.* Fig. 1, gray spectrum). Clearly, the absorption onsets are identical in both solvents; however, in H_2O, a distinct maximum emerges at 248 nm, which is likely also present in DMSO solution. To understand the nature of the underlying electronic transitions, DFT-calculations were conducted. We first optimized the geometry of [**1**] in its singlet electronic ground state and subsequently computed the electronically excited states of the complex at the relaxed S_0-geometry using TD-DFT. The theory returns a stick spectrum (*i.e.* oscillator strength *versus* excitation wavenumber), which was convoluted with a Gaussian line shape function having a half width at half maximum of 4000 cm^{-1} to account for thermal and dynamic solute–solvent line broadening effects in a phenomenological fashion.

The results obtained with the B3LYP/GenECP level of theory (Fig. 1, dashed black curve) agree remarkably well with the experimental data, even without empirically shifting the *in silico* data as

is often done in TD-DFT. Thus, we emphasize that this agreement is fortuitous but nonetheless highly welcome.

Complex, [**1**], is a diamagnetic species having a d^8-configured Pt^{II}-center in a quasi-square-planar coordination sphere. According to the theory, the lowest excited singlet state, S_1, is located at 324 nm corresponding to the Pt-d(z^2) → Pt-d($x^2 - y^2$) electronic promotion (*cf.* Fig. 1(b) and Fig. S1 of the ESI,† for the associated natural transition orbitals[61]). The lowest vertical triplet excitation (dipole forbidden), has the same character and is located at 384 nm. Thus, the vertical singlet–triplet gap at the relaxed singlet ground state geometry amounts to 57.7 kJ mol^{-1}. The absorption onset, and thus, the 248 nm-band distinguished in water, originates almost exclusively from the first excited state that possesses appreciable oscillator strength; *i.e.*, root 8 or S_8, respectively. As shown in Fig. 1(c), this state arises from the metal-to-ligand charge transfer (MLCT), Pt-d(*xz*/*yz*) → ox-π*($2b_{3u}$), where ox = $C_2O_4^{2-}$ in local D_{2h}-symmetry.

In this study, we utilized an excitation wavelength of 266 nm, which is fully in resonance with this strongest MLCT-transition. Such an excitation formally generates a Pt^{III}-center (d^7, $S = \frac{1}{2}$) to which an oxalate radical trianion ($S = \frac{1}{2}$) is anti-ferromagnetically coupled. Having the π*($2b_{3u}$)-orbital singly occupied, the spin density of an isolated $C_2O_4^{\bullet 3-}$ should be delocalized over all six atoms.

The FTIR-spectrum of [**1**] in DMSO solution is displayed in Fig. 2. The spectrum can be divided into two distinct regions; namely, the stretching region of the oxalale's inner C–O-bonds pointing toward the metal center between 1200 cm^{-1} and 1400 cm^{-1}, and that of the outer, dangling C═O-bonds between 1600 cm^{-1} and 1800 cm^{-1}.[62] The inner C–O-stretching motions combine to form an out-of-phase and an in-phase stretching normal mode, which give rise to absorption bands peaking at 1270 cm^{-1} and 1362 cm^{-1}, respectively. The two dangling C═O-stretching vibrations also generate two absorption bands, centered at 1679 cm^{-1} and 1702 cm^{-1}, which can be assigned analogously to their out-of-phase and in-phase stretching normal modes, respectively. The additional weaker absorptions around 1219 cm^{-1} and 1615 cm^{-1} originate from CH_2-wagging and NH_2-bending motions of the diamine ancillary ligand. In the following, we will utilize specifically the oxalate's outer C═O stretching region to derive information about the dynamical processes of [**1**] following its MLCT-excitation at 266 nm.

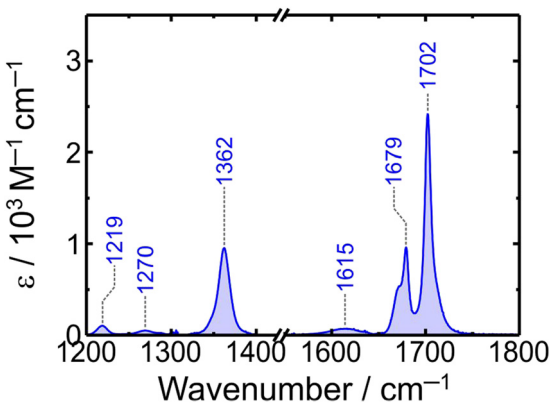

Fig. 2 Experimental FTIR-spectrum of [**1**] in DMSO (blue curve) at room temperature. The numbers indicate the peak positions in cm^{-1}.

UV-pump/IR-probe spectroscopy

Representative 266-nm-pump/MIR-probe spectra of [**1**] in DMSO solution are depicted in Fig. 3 for various time delays. Focusing first on the data recorded in the oxalate's outer C═O-stretching region (left abscissa) immediately after photoexcitation (top spectrum, 400 fs delay), two negative bands peaking at 1678 cm^{-1} and 1702 cm^{-1} are observed. These two signals spectrally coincide with the two absorption bands that were already observed in the same region of the FTIR-spectrum. Hence, they arise from the pump-induced depletion of population of the electronic ground state of [**1**]. The two ground-state bleaching (GSB) bands are accompanied by a broad and structureless positive band peaking at 1634 cm^{-1}. This induced absorption (IA) arises from an electronically excited state of [**1**], presumably the MLCT-state prepared upon absorption of the 266 nm-photon, or alternatively, a lower-lying state that is

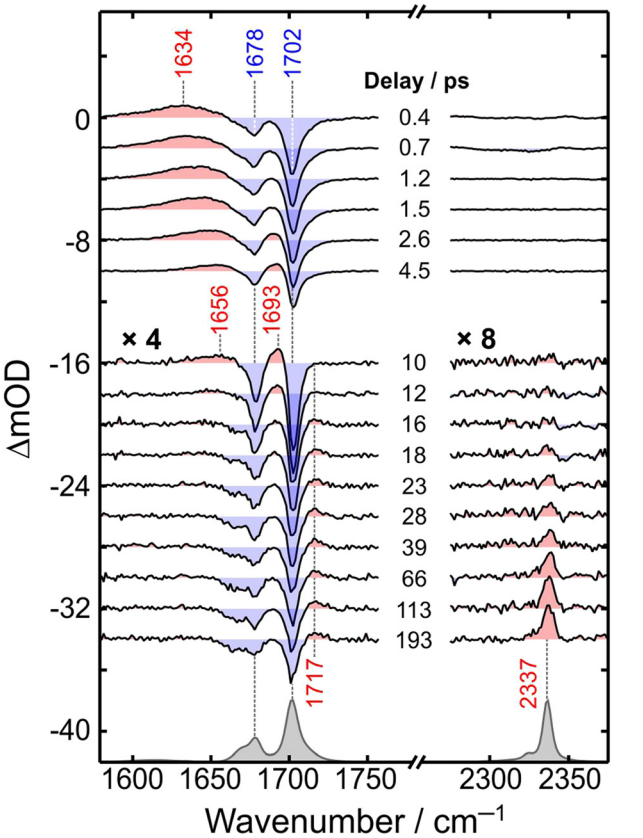

Fig. 3 UV-pump/MIR-probe spectra of [**1**] in DMSO at room temperature for various pump–probe delays. Ground-state bleaching signals are shaded in blue, induced absorption signals are shaded in red. The blue and red numbers indicate peak positions in cm^{-1}. The FTIR spectra of [**1**] and CO_2 in DMSO are shown in gray at the bottom of the figure. Notice that for delays of 10 ps and larger, the spectra in the oxalate's outer C═O stretching region were scaled by a factor of 4, those in the CO_2-region by a factor of 8.

populated upon a non-adiabatic transition occurring within 400 fs.

On a time scale of ~5 ps, the IA-band decays almost completely to zero while spectrally narrowing and shifting by ~22 cm^{-1} towards higher wavenumbers. At the same time, another IA-band emerges in between the two GSB-bands at 1693 cm^{-1}. On even longer time scales of up to 200 ps, the negative bands recover to about 15% of their maximal amplitude (*i.e.*, at a delay of 400 fs). This suggests that *ca.* 85% of all initially excited oxalate complexes return to their electronic ground state whereas 15% are converted into photochemical products of yet to be determined structure. However, the most remarkable UV-pump/MIR-probe signal in the oxalate's outer C═O region is yet another IA-band, which emerges within a few tens of picoseconds at a spectral position of 1717 cm^{-1}; *i.e.*, distinctly upshifted relative to both GSB-bands. This feature is most likely the spectroscopic fingerprint of the photochemical product that is formed with a primary quantum yield of ~15%.

To test whether or not the product is the result of the photoinduced decarboxylation of [**1**] according to Scheme 1, pump–probe experiments were conducted with probe pulses tuned to the antisymmetric stretching absorption of CO_2. The ν_3-mode of the carbonaceous fragment is known to absorb in DMSO-solution at 2337 cm^{-1} (*cf.* Fig. 3, right abscissa, and Fig. S2, ESI†).[50] Indeed, a 266 nm-induced absorption band builds up within ~200 ps at exactly this spectral position. We independently measured the peak extinction coefficient, $\varepsilon(CO_2)$, of the ν_3-absorption of CO_2 and found a value of 1017 M^{-1} cm^{-1} (*cf.* Fig. S2, ESI†). Likewise, the peak extinction coefficient of the 1702 cm^{-1}-band of [**1**] was found to be $\varepsilon([\mathbf{1}])$ = 2424 M^{-1} cm^{-1}. Then, if each oxaliplatin complex, which remains bleached after a delay of 200 ps, cleaved off a carbon dioxide molecule, the amplitude of the ν_3-absorption of CO_2 divided by the bleaching amplitude of [**1**] must be equal to $\varepsilon(CO_2)/\varepsilon([\mathbf{1}])$ = 0.42. From the experimental spectrum recorded at ~200 ps (*cf.* Fig. 3), we derive a ratio of 0.39. The deviation of 7% from the predicted value may easily be due to an imperfect alignment of the pump–probe experiment detecting the CO_2 fragment, the accuracy with which we can determine the extinction coefficient of CO_2, and the bleaching amplitude being diminished because of a partial spectral overlap with an additional product absorption.

Likewise, we can estimate the primary quantum yield, $\Phi(CO_2)$, for CO_2-formation by dividing the asymptotic product's ν_3-absorption, ΔOD (2337 cm^{-1}, $t \geq 193$ ps), by the initial 1702 cm^{-1}-GSB, ΔOD (1702 cm^{-1}, t = 400 fs). Taking into account the two extinction coefficients, we obtain $\Phi(CO_2)$ = (0.28/3.76)·(2424/1017) = 18%, in very good agreement with the value derived above from the final-to-initial 1702 cm^{-1}-GSB ratio. Thus, we can conclude here with confidence that with a primary quantum yield of ~15%, complex [**1**] decomposes upon irradiation with 266 nm-light by releasing one carbon dioxide molecule. Furthermore, the CO_2-loss generates a platinum product complex that absorbs in the outer C═O stretching region near 1717 cm^{-1}.

Before identifying the nature of the product complex, it is instructive to examine the temporal evolution of the individual spectral features identified in Fig. 3. To this end, kinetic traces were extracted from the experimental pump–probe data and the results are displayed in Fig. 4. The trace recorded at the peak of the ν_3-absorption at 2337 cm^{-1} rises in an apparent single-exponential fashion and a least-squares fit returns a time constant of 60 ps (*cf.* panel a and Table S1, ESI†). In contrast, the trace recorded on the blue-shifted IA-band at 1717 cm^{-1} is considerably more complex due to contributions from more than just a single absorbing species (*cf.* Fig. 4(b)). During the

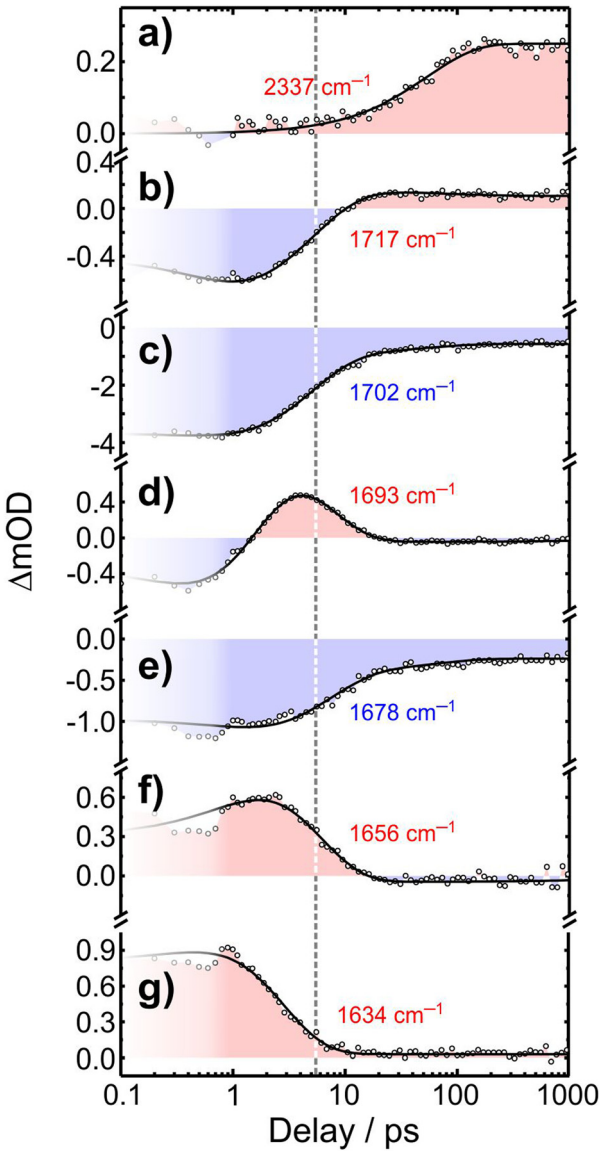

Fig. 4 UV-pump/MIR-probe kinetics traces of [**1**] in DMSO at room temperature for various probe wavenumbers. Open symbols: experimental data, solid curves: fit to multi-exponential kinetics. Absorptive signals are shaded in red, bleaching signals are shaded blue. The delay dependence recorded for delays shorter than 0.5 ps is affected by the coherent artefact. Note the logarithmic delay representation. The vertical dashed line indicates a time delay of 5.5 ps, the recovery time of the electronic ground-state of [**1**].

first 10 ps, the data are dominated by the net bleach of the spectrally adjacent in-phase C═O-stretching absorption as a result of the pump-induced depletion of the electronic ground-state. However, the trace then switches sign to become absorptive for longer delays indicating that the trace is now dominated by the product absorption. The rise time obtained from a multi-exponential least-squares fit is 5.1 ps; *i.e.* an order of magnitude shorter than the build-up of the CO_2-signal.

This ~5 ps-rise time may be due either to the kinetic growth of the product, or alternatively, to the bleach recovery kinetics. To differentiate between these two interpretations, the traces recorded at the two oxalate C═O stretching frequencies are scrutinized in more detail (*cf.* Fig. 4(c) and (e)). For delays in excess of 1 ps, both traces require two exponential components to obtain a satisfactory fit. The dominant contribution to the fit has a time constant of 4.7 ps and 6.5 ps when probing the in-phase (at 1702 cm^{-1}) and out-of-phase (at 1678 cm^{-1}) C═O stretching modes, respectively. These values agree well with the build-up time extracted from the 1717 cm^{-1}-trace, which lets us conclude that the electronic ground-state of [**1**] recovers in (5.5 ± 1.0) ps. The photochemical product absorbing in the C═O-stretching region at 1717 cm^{-1} must either be formed on exactly the same time scale or within the time resolution of the experiment to be consistent with the apparent kinetics at that wavenumber.

To check for consistency, we inspect the kinetics associated with the prompt downshifted induced absorption initially peaking at 1634 cm^{-1} and gradually evolving towards 1656 cm^{-1} (*cf.* Fig. 3 for the pump–probe spectra at early delays). Kinetic traces recorded at these two probe wavenumbers are purely absorptive and are, thus, barely affected the ground-state recovery kinetics. Aside from the earliest delays, which are still affected by the coherent artefact, the kinetic trace recorded at low-frequency edge of the IA-band at 1634 cm^{-1} contains only a continuous decay that can be fitted with an exponential component having a time constant of 2.4 ps (*cf.* Fig. 4(g)). In contrast, the kinetic trace recorded at 1656 cm^{-1} (*cf.* Fig. 4(f)), *i.e.*, at high-frequency edge of the IA-band, initially rises with a time constant of 1.2 ps and subsequently decays with the same time constant of 5.0 ps, which was already observed in the GSB recoveries. We can thus conclude that the downshifted IA-band is caused indeed by one or more electronically excited states of [**1**], which undergo internal conversion to recover the electronic ground state within 5 ps. The rising component in the 1656 cm^{-1}-trace may then be the result of this excited state undergoing vibrational relaxation.

A more accurate time constant of the apparent vibrational relaxation dynamics can be obtained by following the time-dependence of the spectral peak position of the induced absorption. To this end, we fit for each pump–probe delay the IA-band's profile with a fourth-order polynomial and determine its roots in the wavenumber interval between 1620 cm^{-1} and 1660 cm^{-1}. The spectral peak position thus obtained is plotted in Fig. 5 as a function of the pump–probe delay. Clearly, the IA-band shifts to higher wavenumbers in a continuous fashion within only 10 ps. These data can be fitted satisfactorily with a

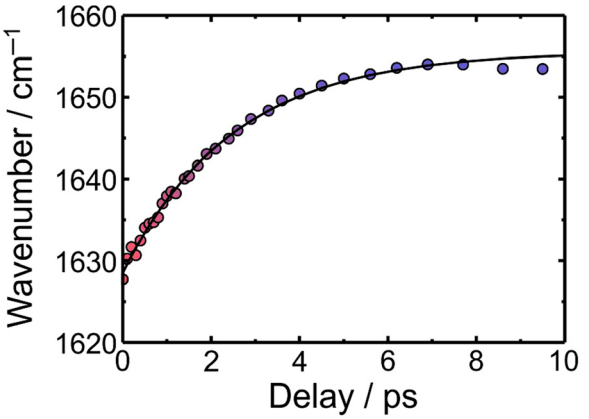

Fig. 5 Peak position of the prompt induced absorption of [**1**] in DMSO (blue curve) at room temperature. The solid curve is a fit to a mono-exponential rise with a time constant of 2.5 ps.

mono-exponential rise having a time constant of 2.5 ps. Thus, the rates of vibrational relaxation and population relaxation of the excited state differ only by a factor of two and consequently, a clear time scale separation between these two distinct processes does not exist. In turn, isosbestic points, which would otherwise be expected for a simple excited state-to-ground state interconversion, are not observed.

At this stage, the question arises from which state the CO_2-fragment is released. Strikingly, the CO_2-signal appears on a time scale of 60 ps, which is actually ten times slower than ground-state recovery. Moreover, any other spectroscopic signal featuring a dominant 60 ps exponential component was not observed. We did detect a minor 50 ps-component in the in-phase and out-of-phase C═O bleaching traces at 1702 cm^{-1} and 1678 cm^{-1}, yet, these components are connected with a negative amplitude indicating that they are related to a population recovery (*cf.* ESI,† Table S1). Thus, they cannot be connected with a release of CO_2 from the electronic ground state of [**1**]. Instead, they could be attributed to the vibrational relaxation of the replenished ground state.

Similarly, we cannot exclude the 60 ps-rise of the antisymmetric stretching absorption of CO_2 to be governed by vibrational relaxation. Indeed, the carbonaceous fragment might actually be born with a high degree of excess vibrational energy as we have observed in previous studies of the decarboxylation dynamics of oxalate complexes of trivalent iron.[43,49–51] In these cases, the absorption of the nascent CO_2 in the ν_3-mode region was enormously broadened because of the anharmonic couplings of the antisymmetric stretching vibration to the symmetric stretch as well as to the two bending modes. These anharmonic couplings between the vibrational degrees of freedom not only broaden the ν_3-region in the presence of vibrational excess energy but they also tend to suppress the peak absorbance for a given number density of CO_2 molecules. Therefore, it is quite likely that if the CO_2-fragment is formed in a highly vibrationally excited state, its absorbance cannot be detected unambiguously due to an insufficient signal-to-noise ratio. A closer inspection of the spectra shown in Fig. 3 suggests

indeed that the ν_3-region is slightly broadened on a time scale of several tens of picoseconds (*cf. e.g.* data collected between 23 ps and 66 ps).

We previously examined, with UV-pump/IR-probe spectroscopy, the photoinduced CO_2-cleavage from the complex, $[Fe^{III}(cyclam)(C_2O_4)]^+$, and used the same DMSO solvent. These two different experiments can therefore be compared directly. As shown in Fig. S3 (ESI†), the rise of the 2337 cm^{-1}-absorption is exactly identical for these two different oxalate complexes. This agreement strongly corroborates the notion that the rise time extracted from the CO_2-signal in Fig. 4(a) corresponds to the vibrational relaxation time of the triatomic fragment. Notice that the vibrational relaxation time of 60 ps is derived by phenomenologically fitting the experimental data in the time domain only. A more accurate relaxation time that is footed on a realistic molecular model for vibrational cooling, taking into account prior knowledge of the full set of anharmonic couplings involving the ν_3-mode, can be derived according to ref. 50,51. Notice also that a phenomenological relaxation time of 60 ps is a factor of 2.7 longer than the lifetime of the $n = 1$ state of the antisymmetric stretching mode as determined from an independent IR-pump/IR-probe experiment exciting the ν_3-fundamental transition of CO_2 in DMSO (22.5 ps, *cf.* Fig. S3, ESI†).

Photoinduced processes, excited states, and products

Having verified that CO_2 is released and that it appears to thermalize within 60 ps after photoexcitation of the oxalate parent complex, the identity of the metal-containing co-fragment, presumably a carbon dioxide complex of platinum, needs to be clarified. In addition, the origin of the two induced absorptions must be assigned. To this end, the molecular, electronic, and vibrational structures of [**1**] are scrutinized in more detail first. Since the dynamics are optically induced and internal conversions as well as intersystem crossings may play a pivotal role in the primary processes, such information is needed for both, the singlet and the triplet electronic manifolds.

On the singlet ground-state surface ($S = 0$), the DFT-calculations (B3LYP/GenECP) actually reveal two distinct geometric isomers; namely, the expected $\kappa^2(O^1,O^2)$ binding mode, which coordinates the oxalate ligand through a pair of vicinal oxygen atoms to the platinum center, and the $\kappa^2(O^1,O^{1'})$ binding mode connecting the oxalate *via* two geminal O-atoms to the Pt-ion (*cf.* Fig. 6, structures a and b). The $\kappa^2(O^1,O^2)$ binding mode is 87.4 kJ mol^{-1} more stable than the $\kappa^2(O^1,O^{1'})$-structure. As a result, the latter is thermally inaccessible at 300 K and can therefore not contribute to the IR-spectrum. As shown in Fig. 7(a), the theory predicts for the $\kappa^2(O^1,O^2)$-isomer that its in-phase outer C═O-stretching mode absorbs at 1714 cm^{-1}, in very good agreement with the experimental observation (1702 cm^{-1}). A spectral splitting of 15 cm^{-1} between the two outer C═O stretching normal modes of the $\kappa^2(O^1,O^2)$-isomer is predicted by the calculation, which is only 9% smaller than determined experimentally. However, DFT is unable to accurately reproduce the intensity ratio between the in-phase and out-of-phase dangling C═O-bands, a shortcoming we have noted previously in a benchmark study[49,50] for a large variety of exchange–correlation functionals. The in-phase inner C–O stretching mode of the $\kappa^2(O^1,O^2)$-isomer is located by the theory at 1366 cm^{-1}, which lines up almost perfectly with the corresponding FTIR-resonance (1362 cm^{-1}, *cf.* Fig. 2). Based on this good agreement between the experimental FTIR-spectrum and the corresponding DFT-prediction we can conclude that the chosen model chemistry, B3LYP/GenECP, provides again very accurate vibrational frequencies in the oxalate stretching region and that it can be used to reliably predict the IR-spectra of hypothetical intermediates and/or products emerging from the electronic excitation of [**1**].

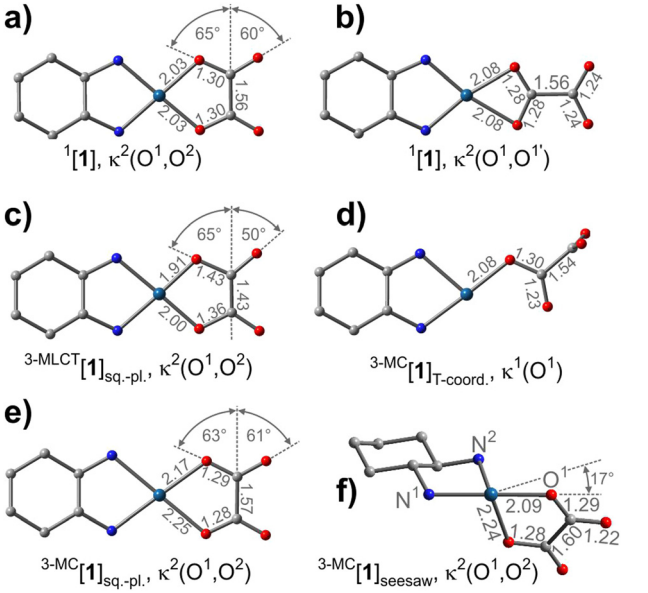

Fig. 6 DFT-optimized molecular structures of oxaliplatin in the singlet electronic ground state (a, b) and various triplet excited states (c through f). The seesaw structure in (f) is oriented in such a way that the apical axis (N^1–Pd–O^1) lies horizontally and the equatorial vacancy points out of the paper plane towards the reader's eye. Level-of-theory: restricted ($S = 0$) and unrestricted ($S = 1$) B3LYP/GenECP. H-atoms hidden for clarity. All other atoms color-coded as follows: gray = C, blue = N, pale blue = Pt, red = O. Numbers indicate important structural parameters (bond lengths and angles).

The excited states of [**1**] in both, the singlet and triplet electronic manifolds need to be explored next. To this end, geometry optimizations were initially conducted with unrestricted DFT and a total spin, $S = 1$ (spin triplets). Surprisingly, four different structures were found; one of which is a metal-to-ligand charge transfer (MLCT) state and the other three are metal-centered states. The MLCT moves an electron from the d_{xz}-orbital of the Pt-center to the $3b_{3u}$-orbital of the planar oxalate dianion (local symmetry D_{2h}). The latter is π-antibonding with respect to the ligand's four CO-bonds, but it is π-bonding regarding the central CC-bond. As a result, the MLCT-state geometrically relaxes by extending the oxalate's CO-bonds and contracting the CC-bond. Moreover, the resultant trianionic ligand, $C_2O_4^{\bullet 3-}$, bound to a Pt^{III}-ion suffers also from an asymmetric distortion ultimately resulting in a quasi-square-planar coordination geometry, which entails a $\kappa^2(O^1,O^2)$-bound oxalate having two different inner C–O bond distances and

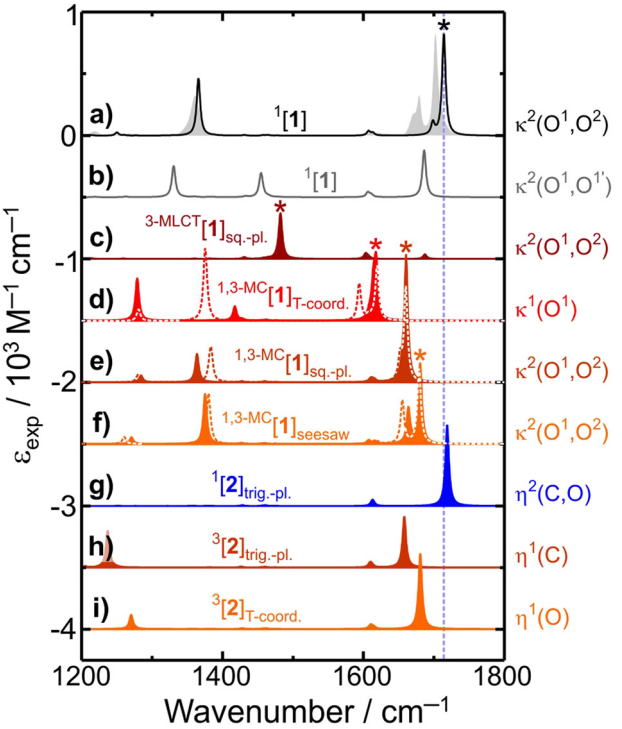

Fig. 7 DFT-predicted IR-spectra of oxaliplatin ([**1**]) and its decarboxylation product ([**2**]) in their geometry-optimized ground and excited states. The relaxed structure is indicated by the ligand sphere geometry and the binding mode of the carbonaceous ligands, oxalate and carbon dioxide, respectively. In the outer CO-stretching region between 1600 cm^{-1} and 1800 cm^{-1}, the only species whose absorption is upshifted relative to the parent ground state is the side-on carbon dioxide complex (blue). All other species absorb downshifted. Level-of-theory: restricted (S = 0) and unrestricted (S = 1) B3LYP/GenECP. The asterisks mark the strongest dangling C═O stretching band for each oxalate bearing species. The dashed curves in (d) and (f) represent the DFT-predicted spectra of the equivalent singlet excited states. The gray shaded spectrum in (a) represents the experimental FTIR-spectrum.

non-equivalent Pt–O coordination bonds (*cf.* Fig. 6, structure c). We denote this state as $^{3\text{-MLCT}}$[**1**]$_{\text{sq.-pl.}}$. As a result of the ligand's symmetry breakage, the in-phase dangling C═O-stretching motion becomes nearly IR-silent whereas the out-of-phase motion becomes strongly IR-allowed; quite in contrast to the ground state's outer C═O normal modes. Apart from this intensity reversal, the absorption of the out-of-phase combination now shifts by more than 200 cm^{-1} to lower wavenumbers relative to that of the ground state (*cf.* Fig. 7(c)), thus, highlighting the reduced bond order of the dangling CO-groups.

The state, $^{3\text{-MLCT}}$[**1**]$_{\text{sq.-pl.}}$, lies 324.8 kJ mol^{-1} above the relaxed ground state and is thus energetically accessible upon excitation with a 266 nm-photon (equivalent to 449.7 kJ mol^{-1}). Somewhat lower in energy (241.3 kJ mol^{-1} above ^{1}[**1**]) is a metal-centered triplet state, denoted here as $^{3\text{-MC}}$[**1**]$_{\text{T-coord.}}$, that arises from the Pt-centered d_{z^2}-to-$d_{x^2-y^2}$ electronic promotion. Its structure is connected with a T-shaped coordination sphere containing a monodentate oxalate ligand, which in turn is twisted about its CC-bond and is thus reminiscent of the free oxalate dianion (see structure d in Fig. 6). Not surprisingly, its IR-spectrum is very similar to that of free $C_2O_4^{2-}$ with its two (almost) degenerate antisymmetric O–C═O stretching modes (species E in local D_{2d}-symmetry). According to the theory their absorption is downshifted by 96 cm^{-1} relative to the principal dangling C═O-stretching absorption of the ground state (see Fig. 7(d)).

Interestingly, $^{3\text{-MC}}$[**1**]$_{\text{T-coord}}$ is just one out of two structural isomers, which exist on the adiabatic triplet potential energy surface associated with the d_{z^2}-to-$d_{x^2-y^2}$ electronic excitation. The second isomer, denoted here $^{3\text{-MC}}$[**1**]$_{\text{sq.-pl.}}$, features the intuitively expected square-planar ligand sphere with a $\kappa^2(O^1,O^2)$-bound oxalate (*cf.* structure e in Fig. 6). It is located at an energy of 221.0 kJ mol^{-1} above the electronic ground state and exhibits a dominant dangling C═O-stretching absorption that is downshifted by 54 cm^{-1} relative to that of the ground state (*cf.* Fig. 7(e)). An overview of the energetics derived from DFT and TD-DFT is presented in Fig. S4 (*cf.* ESI†).

Finally, the global triplet ground state, labeled from hereon $^{3\text{-MC}}$[**1**]$_{\text{seesaw}}$, is located at an energy of 184.6 kJ mol^{-1} above the minimum energy structure of the singlet ground state surface. It features an unexpected coordination sphere, as depicted in Fig. 6(f). The structure resembles a twisted seesaw; *i.e.* a distorted trigonal-bipyramid with an equatorial vacancy. The three collinear atoms O^1–Pt–N^1 define the apical axis (the seesaw's lever) while the bend angle, O^2–Pt–N^2 (the seesaw's fulcrum) lies within the equatorial plane. The plane's normal is tilted with respect to the apical axis by 17 degrees. At the same time, the oxalate ligand itself remains fully planar and oriented perpendicular to the diamine plane. A structural relaxation from square-planar to seesaw coordination swaps the highest occupied and the lowest unoccupied molecular orbitals (HOMO ↔ LUMO). In the seesaw coordination, the $d_{x^2-y^2}$-orbital becomes the HOMO and the d_{z^2}-orbital becomes the LUMO. Consequently, the $^{3\text{-MC}}$[**1**]$_{\text{seesaw}}$-state arises from the Pt-centered $d_{x^2-y^2}$-to-d_{z^2} electronic promotion; quite in contrast to the $^{3\text{-MLCT}}$[**1**]$_{\text{sq.-pl.}}$ and $^{3\text{-MC}}$[**1**]$_{\text{T-ccord.}}$-states.

Importantly, the dominant absorption of the out-of-phase C═O-stretching combination of the $^{3\text{-MC}}$[**1**]$_{\text{seesaw}}$-state is predicted to be downshifted by only 34 cm^{-1} relative to that of the ground state *cf.* Fig. 7(f). Thus, according to the theory there is a very clear correlation between the electronic energy of the excited states and the wavenumber of their strongest dangling C═O stretching vibration. The energy decreases in the order $^{3\text{-MLCT}}$[**1**]$_{\text{sq.-pl.}}$ > $^{3\text{-MC}}$[**1**]$_{\text{T-ccord.}}$ > $^{3\text{-MC}}$[**1**]$_{\text{sq.-pl.}}$ > $^{3\text{-MC}}$[**1**]$_{\text{seesaw}}$ > [**1**] while, as is highlighted by the asterisks in Fig. 7, the wavenumber increases in that order (1482 cm^{-1} > 1618 cm^{-1} > 1660 cm^{-1} > 1680 cm^{-1} > 1714 cm^{-1}, spectra c through f and a).

To obtain information of the singlet excited states (*i.e.* di-radical states), TD-DFT and broken-symmetry DFT-calculations were carried out next (*cf.* ESI† for detailed structural data of these species). These computations reveal a fully complementary trend for the excited states in the singlet electronic manifold (*cf.* dashed spectra in Fig. 6). Therefore, the pronounced blue-shift of the induced C═O stretching absorption observed

during the first few picoseconds after UV-excitation of [**1**] (*cf.* Fig. 5) may also reflect an electronic downhill relaxation from the initially prepared singlet excited state toward the lowest singlet and triplet excited states, $^{1\text{-MC}}[\mathbf{1}]_{\text{seesaw}}$ and $^{3\text{-MC}}[\mathbf{1}]_{\text{seesaw}}$. In addition, these states will be dressed with vibrational excess energy, which will randomize within the molecule by intramolecular vibrational redistribution and which will eventually dissipate by vibrational energy transfer into the solvent. As alluded to above, vibrational relaxation then also contributes to the dynamic spectral upshift of the induced C═O stretching absorption.

Having found a satisfactory interpretation of the induced absorption appearing downshifted relative to the parent bleaching band, we now focus on the assignment of the upshifted absorption peaking in Fig. 3 at 1717 cm^{-1}. To this end, the molecular, electronic, and vibrational structures of [**2**], *i.e.* of the Pt-containing primary product, must be investigated. Geometry optimizations were therefore conducted on both, the singlet and the triplet potential energy surfaces of the species Pt(dach)(CO_2), and the main results are depicted in Fig. 8.

On the singlet surface, $S = 0$, with restricted DFT, only one minimum was found corresponding to a geometry with the CO_2-ligand ligating to the metal in the $\eta^{(2)}_{C,O}$-motif (or "side-on" mode, Fig. 8(a)). The coordination geometry can be regarded as trigonal planar and, hence, we denote this structure as $^{1}[\mathbf{2}]_{\text{trig.-pl.}}$. Except for the heavier group-10 metal (Pt) and the ancillary ligand (dach), this is exactly the structure, which was reported by Aresta in his seminal papers on $[Ni(CO_2)(PCy_3)_2]$.[47,48]

With unrestricted DFT and a total spin, $S = 1$, two different geometries were discovered; namely, $\eta^{(1)}_{C}$ (or "Y-on" mode, *cf.* Fig. 8(b), $^{3}[\mathbf{2}]_{\text{trig.-pl.}}$) and $\eta^{(1)}_{O}$ (or "end-on" mode, Fig. 8(c), $^{3}[\mathbf{2}]_{\text{T-coord.}}$). In the former case, the coordination geometry is trigonal planar whereas in the latter case, it is T-shaped. In both cases, however, the carbon dioxide ligand adopts a bent geometry indicating an occupation of a low-lying π*-orbital of the triatomic unit. While in the $\eta^{(1)}_{C}$-structure, the triatomic ligand is fully aligned within the coordination plane, it is distinctly oriented out-of-plane in the $\eta^{(1)}_{O}$-structure. In either case, an inspection of the spin density reveals that the electronic structure of the complex is best described by a $CO_2^{\bullet-}$ radical anion ligand ($S = \frac{1}{2}$), which is ferromagnetically coupled to a Pt^{I}-center (d^9, $S = \frac{1}{2}$) to create the overall spin triplet, $S = 1$ (*cf.* ESI† for structural data and spin density plots).

However, DFT predicts [**2**] to be a diamagnetic complex, *i.e.*, $^{1}[\mathbf{2}]_{\text{trig.-pl.}}$ with the side-on mode is the electronic ground state – just like in the case of Aresta's paradigmatic model complex.[47,48] Its formation by CO_2-loss from the oxalate precursor according to Scheme 1 requires an energy of only 56.3 kJ mol^{-1} and when taking into account thermal excitation, the reaction becomes even weakly exergonic at room temperature (ΔG = −3.4 kJ mol^{-1}, model chemistry B3LYP/GenECP). Clearly, [**1**] is a thermally stable compound, and as such, its decarboxylation reaction must be inhibited by a very large barrier. Of the two triplet geometries, $^{3}[\mathbf{2}]_{\text{trig.-pl.}}$ with the Y-on motif is energetically lower. It lies 145.8 kJ mol^{-1} above the side-on structure, but 61.0 kJ mol^{-1} below $^{3}[\mathbf{2}]_{\text{T-coord.}}$ with the bent O-on binding mode.

The DFT-predicted IR-spectra for the three geometry-optimized structures of [**2**] are displayed in Fig. 7(g) though Fig. 7(i). According to the theory, the two triplet species carry a $CO_2^{\bullet-}$ ligand. Zhou and Andrews[63] reported the IR-spectrum of the radical anion in a cryogenic matrix and its asymmetric stretching absorption was located at 1660 cm^{-1}. The theory predicts this vibration to absorb at 1658 cm^{-1} and 1681 cm^{-1} for the Y-on and bent-O-end-on triplet complex, respectively, thereby confirming the open–shell nature of the triatomic ligand. Note that both species absorb downshifted relative to the principal dangling C═O stretching mode of the parent, $^{1}[\mathbf{1}]$.

In contrast, the side-on singlet complex, $^{1}[\mathbf{2}]_{\text{trig.-pl.}}$, is predicted to absorb at 1719 cm^{-1}, *i.e.* at much higher wavenumbers and even noticeably upshifted with regard to $^{1}[\mathbf{1}]$ (*cf.* the blue spectrum, Fig. 7(g)). Therefore, in the carbonyl region, $^{1}[\mathbf{2}]_{\text{trig.-pl.}}$ is spectroscopically reminiscent of an aliphatic ketone. The electronic structure of the side-on binding mode of [**2**] can be understood intuitively by reviewing the natural bond orbitals (NBOs)[64] associated with the Pt($\eta^{(2)}_{C,O}$-CO_2)-moiety (*cf.* Fig. S5, ESI†). It turns out that carbon dioxide moiety is attached to the metal center through its terminal O^1-atom by a σ-bond involving a 6p5d-hybrid at the Pt and an oxygen's in-plane p-orbital. Similarly, σ-bonding between the metal and the central C-atom is accomplished with a Pt-6s5d-hybrid and a carbon's sp^2-hybrid. Just like in an organic ketone, the dangling $C{=}O^2$ unit is held together by a σ-bond comprising an sp^2-hybrid on each atom and a π-bond containing the two atom's p_z-orbitals, thereby giving rise to a classical bond order of two. This leaves a total of four lone pairs residing in the O^1-p_z-orbital, the in-plane O^2-p-orbital, and an sp-hybrid on each of the two oxygens. According to this binding pattern, the $^{1}[\mathbf{2}]_{\text{trig.-pl.}}$ structure may be interpreted as a metalla-α-lactone or more accurately, as 1-oxa-3-platinacyclopropan-2-one; a three-membered heterocycle featuring a $5d^9 6(sp)^1$-natural electron-configured platinum(0) center and an exocyclic ketone-like carbonyl bond.[65] However, we emphasize here that this intuitive notion comes with the caveat that the metal contributes significantly less than 50% to the σ-bond connecting it to O^1

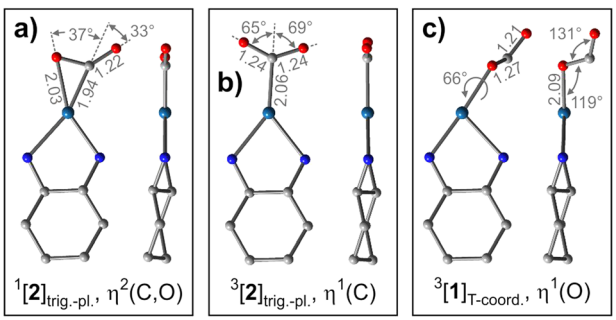

Fig. 8 DFT-optimized molecular structures of (carbon dioxide)[(1*R*,2*R*)-cyclohexanediamine]platinum(II) ([**2**]) in the singlet ground state (panel a) and the triplet states (panels b and c). In structure (a), the OCO bend angle is 133°. Level-of-theory: restricted ($S = 0$) and unrestricted ($S = 1$) B3LYP/GenECP. H-atoms hidden for clarity. All other atoms color-coded as follows: gray = C, blue = N, pale blue = Pt, red = O.

(*cf.* Fig. S5, ESI†). This observation may indicate a need for a multi-reference approach to describe the electronic structure of [**2**] correctly.[46]

Upon revisiting the results compiled in Fig. 7 one realizes that the IR-spectrum predicted for the side-on product complex, $^{1}[\mathbf{2}]_{\text{trig.-pl}}$, is quite unique. This is because it is actually the only spectrum that exhibits a C═O stretching absorption, which is upshifted relative to the dominant C═O stretching absorption of oxaliplatin (*cf.* spectra g and a). In other words, of all the species whose molecular and electronic structure we were able to disentangle, the CO_2–Pt complex, $^{1}[\mathbf{2}]_{\text{trig.-pl}}$ in its singlet electronic ground state with the $\eta^{(2)}_{C,O}$-binding motif, is the only species that can be held responsible for the experimentally observed upshifted induced absorption peaking at 1717 cm^{-1}. All other species are predicted to have downshifted absorptions only. Thus, we conclude here that upon 266 nm-excitation, oxaliplatin decarboxylates on a time scale of 5 ps (or shorter) and generates with a quantum yield of ~15% a closed–shell carbon dioxide complex of platinum, a platina-α-lactone, as a photochemical product that is stable for at least 1 ns (the longest delay used in this study). We did notice, however, that over the course of the pump–probe experiment of ~1 hour, a deposit on the sample cell windows was formed, which could be $^{1}[\mathbf{2}]_{\text{trig.-pl}}$ itself or its degradation product, *e.g.* Pt(dach)$(DMSO)_2$. We are currently attempting to observe the delayed buildup of carbon dioxide using rapid scan FTIR-spectroscopy to clarify such a hypothesis. Finally, we briefly refer to a complete active space self consistent field (CASSCF) calculation, we carried out on the smaller model system, ($\eta^{(2)}_{C,O}$-carbon dioxide)(ethylene diamine)platinum, to test the reliability of the above DFT-results. A total of 18 valence electrons were correlated in an active space consisting of 12 orbitals (*cf.* ESI,† Fig. S6). An analysis of the converged CASSCF-wave function does in fact corroborate our interpretation of the photochemical product as a heterocyclic ketone containing a platinum(0) center.

Conclusions

In summary, we have studied the photoinduced decarboxylation of oxaliplatin in liquid solution using time-resolved UV-pump/mid-infrared-probe spectroscopy. The study was motivated by our initial goal to access photochemically a congener of Aresta's celebrated group-10 transition metal carbon dioxide complex featuring the side-on binding mode. The UV/mid-IR data combined with detailed DFT-calculations revealed indeed that after 266 nm-excitation, oxaliplatin releases a neutral single carbon dioxide molecule to form the sought species, (carbon dioxide)[(1*R*,2*R*)-cyclohexanediamine]platinum ([**2**]). This product reveals itself unambiguously by its characteristic dangling carbonyl stretching absorption; a spectroscopic marker, which is upshifted compared to the principal oxalate stretching absorption of the parent. The dangling C═O stretching vibration of [**2**] thus appears in the C═O stretching region of aliphatic ketones; *i.e.* around 1717 cm^{-1}. The IR-spectroscopic properties of [**2**] in the carbonyl region can be traced back to the electronic structure associated with the side-on mode of binding of the carbon dioxide ligand to the platinum center. An NBO-analysis revealed that the product can indeed be viewed in simple terms as a platina-α-lactone; *i.e.* an exocyclic ketone featuring an oxygen and a platinum(0) center in a three-membered ring. This highly intriguing product complex appears on a time scale of 5 ps after photoexcitation. Owing to the limited time resolution of the UV/mid-IR set-up, it remains unclear at this stage whether the CO_2-fragment is expelled from an excited state of the oxalate parent or immediately upon return to the hot electronic ground state *via* internal conversion or intersystem crossing. We are therefore currently engaged in additional UV-pump/while-light probe experiments with a significantly superior time-resolution (~50 fs) and probe the electronic degrees of freedom of the dynamically evolving system. Such studies will hopefully reveal spectroscopic fingerprints of the optically prepared MLCT-excited state as well as lower lying singlet and triplet electronic excitations that might be transiently occupied.

Data availability

The data supporting this article have been included as part of the ESI.† All data available from the authors upon reasonable request.

Conflicts of interest

There are no conflicts to declare.

Acknowledgements

Financial support by the German Research Foundation, grant number 397162618, is gratefully acknowledged.

Notes and references

1 A. Bazzanella and D. Krämer, *Technologies for Sustainability and Climate Protection – Chemical Processes and Use of CO_2,* DECHEMA Gesellschaft für Chemische Technik und Biotechnologie e. V., Frankfurt/Main, 2017.
2 H. Arakawa, M. Aresta, J. N. Armor, M. A. Barteau, E. J. Beckman, A. T. Bell, J. E. Bercaw, C. Creutz, E. Dinjus, D. A. Dixon, K. Domen, D. L. DuBois, J. Eckert, E. Fujita, D. H. Gibson, W. A. Goddard, D. W. Goodman, J. Keller, G. J. Kubas, H. H. Kung, J. E. Lyons, L. E. Manzer, T. J. Marks, K. Morokuma, K. M. Nicholas, R. Periana, L. Que, J. Rostrup-Nielson, W. M. H. Sachtler, L. D. Schmidt, A. Sen, G. A. Somorjai, P. C. Stair, B. R. Stults and W. Tumas, *Chem. Rev.*, 2001, **101**, 953–996.
3 M. Aresta and A. Dibenedetto, *Dalton Trans.*, 2007, 2975–2992.
4 M. Aresta and A. Dibenedetto, in *Developments and Innovation in Carbon Dioxide (CO2) Capture and Storage Technology*, ed. M. M. Maroto-Valer, Woodhead Publishing, 2010, vol. 2, pp. 377–410.

5 M. Aresta, *Carbon Dioxide as a Chemical Feedstock*, Wiley-VCH Verlag, Weinheim, 2010.
6 M. Mikkelsen, M. Jørgensen and F. C. Krebs, *Energy Environ. Sci.*, 2010, **3**, 43–81.
7 M. Aresta, in *Activation of Small Molecules. Organometallic and Bioinorganic Perspectives*, ed. W. B. Tolman, Wiley-VCH, Weinheim, 2006, pp. 1–41.
8 S. Dabral and T. Schaub, *Adv. Synth. Catal.*, 2019, **361**, 223–246.
9 T. Sakakura, J. C. Choi and H. Yasuda, *Chem. Rev.*, 2007, **107**, 2365–2387.
10 D. R. Burgess Jr., in *NIST Chemistry WebBook, NIST Standard Reference Database Number 69*, ed. P. J. Linstrom, W. G. Mallard, National Institute of Standards and Technology, Gaithersburg MD, 2024, p. 20899.
11 M. L. Alcantara, K. A. Pacheco, A. E. Bresciani and R. M. B. Alves, *Ind. Eng. Chem. Res.*, 2021, **60**, 9246–9258.
12 Z. Jiang, T. Xiao, V. L. Kuznetsov and P. P. Edwards, *Philos. Trans. R. Soc. London, Ser. A*, 2010, **368**, 3343–3364.
13 X. L. Zhang, S. X. Guo, K. A. Gandionco, A. M. Bond and J. Zhang, *Mater. Today Adv.*, 2020, **7**, 100074.
14 J. Resasco and A. T. Bell, *Trends Chem.*, 2020, **2**, 825–836.
15 Y. Hori, in *Modern Aspects of Electrochemistry*, ed. C. G. Vayenas, R. E. White and M. E. Gamboa-Aldeco, Springer, New York, New York, NY, 2008, pp. 89–189.
16 R. Cauwenbergh and S. Das, *Green Chem.*, 2021, **23**, 2553–2574.
17 A. Rosas-Hernández, H. Junge and M. Beller, *ChemCatChem*, 2015, **7**, 3316–3321.
18 B. Kumar, M. Llorente, J. Froehlich, T. Dang, A. Sathrum and C. P. Kubiak, *Annu. Rev. Phys. Chem.*, 2012, **63**, 541–569.
19 G. H. Han, J. Bang, G. Park, S. Choe, Y. J. Jang, H. W. Jang, S. Y. Kim and S. H. Ahn, *Small*, 2023, **19**, 2205765.
20 A. Ünlü, Z. E. Duman-Özdamar, B. Çaloglu and B. Binay, *Protein J.*, 2021, **40**, 489–503.
21 A. Nisar, S. Khan, M. Hameed, A. Nisar, H. Ahmad and S. A. Mehmood, *Microbiol. Res.*, 2021, **251**, 126813.
22 I. Bernhardsgrütter, G. M. M. Stoffel, T. E. Miller and T. J. Erb, *Curr. Opin. Biotechnol.*, 2021, **67**, 80–87.
23 S. M. Glueck, S. Gümüs, W. M. F. Fabian and K. Faber, *Chem. Soc. Rev.*, 2010, **39**, 313–328.
24 S. J. Poormohammadian, F. Bahadoran and G. R. Vakili-Nezhaad, *Rev. Chem. Eng.*, 2023, **39**, 783–805.
25 S. Kar, J. Kothandaraman, A. Goeppert and G. K. S. Prakash, *J. CO2 Util.*, 2018, **23**, 212–218.
26 Y. N. Li, R. Ma, L. N. He and Z. F. Diao, *Catal. Sci. Technol.*, 2014, **4**, 1498–1512.
27 P. G. Jessop, T. Ikariya and R. Noyori, *Chem. Rev.*, 1995, **95**, 259–272.
28 A. M. Appel, J. E. Bercaw, A. B. Bocarsly, H. Dobbek, D. L. DuBois, M. Dupuis, J. G. Ferry, E. Fujita, R. Hille, P. J. A. Kenis, C. A. Kerfeld, R. H. Morris, C. H. F. Peden, A. R. Portis, S. W. Ragsdale, T. B. Rauchfuss, J. N. H. Reek, L. C. Seefeldt, R. K. Thauer and G. L. Waldrop, *Chem. Rev.*, 2013, **113**, 6621–6658.
29 X. Jiang, X. W. Nie, X. W. Guo, C. S. Song and J. G. G. Chen, *Chem. Rev.*, 2020, **120**, 7984–8034.
30 S. Mirzakhani, B. H. Yin, M. Masteri-Farahani and A. C. K. Yip, *ChemPlusChem*, 2023, **88**, e202300157.
31 P. Gao, L. N. Zhang, S. G. Li, Z. X. Zhou and Y. H. Sun, *ACS Central Sci.*, 2020, **6**, 1657–1670.
32 J. W. Zhong, X. F. Yang, Z. L. Wu, B. L. Liang, Y. Q. Huang and T. Zhang, *Chem. Soc. Rev.*, 2020, **49**, 1385–1413.
33 X. L. Yin and J. R. Moss, *Coord. Chem. Rev.*, 1999, **181**, 27–59.
34 D. H. Gibson, *Chem. Rev.*, 1996, **96**, 2063–2095.
35 D. H. Gibson, *Coord. Chem. Rev.*, 1999, **185–6**, 335–355.
36 W. Leitner, *Coord. Chem. Rev.*, 1996, **153**, 257–284.
37 T. Fan, X. H. Chen and Z. Y. Lin, *Chem. Commun.*, 2012, **48**, 10808–10828.
38 A. Paparo and J. Okuda, *Coord. Chem. Rev.*, 2017, **334**, 136–149.
39 M. Cokoja, C. Bruckmeier, B. Rieger, W. A. Herrmann and F. E. Kuhn, *Angew. Chem., Int. Ed.*, 2011, **50**, 8510–8537.
40 U. Burghaus, *Prog. Surf. Sci.*, 2014, **89**, 161–217.
41 A. L. Beckwith and R. O. C. Norman, *J. Chem. Soc. B*, 1969, 400–403.
42 D. Schröder, C. A. Schalley, J. N. Harvey and H. Schwarz, *Int. J. Mass Spectrom.*, 1999, **185**, 25–35.
43 S. Straub, P. Brünker, J. Lindner and P. Vöhringer, *Angew. Chem., Int. Ed.*, 2018, **57**, 5000–5005.
44 C. Jegat, M. Fouassier, M. Tranquille, J. Mascetti, I. Tommasi, M. Aresta, F. Ingold and A. Dedieu, *Inorg. Chem.*, 1993, **32**, 1279–1289.
45 A. Paparo and J. Okuda, *J. Organomet. Chem.*, 2018, **869**, 270–274.
46 K. Blaziak, D. Tzeli, S. S. Xantheas and E. Uggerud, *Phys. Chem. Chem. Phys.*, 2018, **20**, 25495–25505.
47 M. Aresta, C. F. Nobile, V. G. Albano, E. Forni and M. Manassero, *J. Chem. Soc., Chem. Commun.*, 1975, 636–637.
48 M. Aresta and C. F. Nobile, *J. Chem. Soc., Dalton Trans.*, 1977, 708–711.
49 S. Straub and P. Vöhringer, *Angew. Chem., Int. Ed.*, 2021, **60**, 2519–2525.
50 S. Straub and P. Vöhringer, *Phys. Chem. Chem. Phys.*, 2021, **23**, 17826–17835.
51 S. Straub, P. Brünker, J. Lindner and P. Vöhringer, *Phys. Chem. Chem. Phys.*, 2018, **20**, 21390–21403.
52 P. Vöhringer, *Dalton Trans.*, 2020, **49**, 256–266.
53 L. I. Domenianni, M. Bauer, T. Schmidt-Räntsch, J. Lindner, S. Schneider and P. Vöhringer, *Angew. Chem., Int. Ed.*, 2023, **62**, e202309618.
54 M. J. Frisch, G. W. Trucks, H. B. Schlegel, G. E. Scuseria, M. A. Robb, J. R. Cheeseman, G. Scalmani, V. Barone, G. A. Petersson, H. Nakatsuji, X. Li, M. Caricato, A. V. Marenich, J. Bloino, B. G. Janesko, R. Gomperts, B. Mennucci, H. P. Hratchian, J. V. Ortiz, A. F. Izmaylov, J. L. Sonnenberg, D. Williams, F. Ding, F. Lipparini, F. Egidi, J. Goings, B. Peng, A. Petrone, T. Henderson, D. Ranasinghe, V. G. Zakrzewski, J. Gao, N. Rega, G. Zheng, W. Liang, M. Hada, M. Ehara, K. Toyota, R. Fukuda, J. Hasegawa, M. Ishida, T. Nakajima, Y. Honda, O. Kitao, H. Nakai, T. Vreven, K. Throssell, J. A. Montgomery Jr., J. E. Peralta, F. Ogliaro, M. J. Bearpark, J. J. Heyd, E. N. Brothers,

K. N. Kudin, V. N. Staroverov, T. A. Keith, R. Kobayashi, J. Normand, K. Raghavachari, A. P. Rendell, J. C. Burant, S. S. Iyengar, J. Tomasi, M. Cossi, J. M. Millam, M. Klene, C. Adamo, R. Cammi, J. W. Ochterski, R. L. Martin, K. Morokuma, O. Farkas, J. B. Foresman and D. J. Fox, Gaussian, Inc., Wallingford, CT, 2016.
55 S. Hirata and M. Head-Gordon, *Chem. Phys. Lett.*, 1999, **314**, 291–299.
56 A. D. Becke, *J. Chem. Phys.*, 1993, **98**, 5648–5652.
57 S. Grimme, J. Antony, S. Ehrlich and H. Krieg, *J. Chem. Phys.*, 2010, **132**, 154104.
58 F. Weigend and R. Ahlrichs, *Phys. Chem. Chem. Phys.*, 2005, **7**, 3297–3305.
59 D. Andrae, U. Häußermann, M. Dolg, H. Stoll and H. Preuß, *Theor. Chim. Acta*, 1990, **77**, 123–141.
60 V. Barone and M. Cossi, *J. Phys. Chem. A*, 1998, **102**, 1995–2001.
61 R. L. Martin, *J. Chem. Phys.*, 2003, **118**, 4775–4777.
62 K. Nakamoto, *Infrared and Raman Spectra of Inorganic and Coordination Compounds*, John Wiley & Sons Inc., Hoboken, NJ, 2009.
63 M. F. Zhou and L. Andrews, *J. Chem. Phys.*, 1999, **110**, 2414–2422.
64 C. R. Landis and F. Weinhold, *The Chemical Bond*, 2014, pp. 91–120.
65 Larger metallalactones with more than three atoms in the heterocycle have been reported before. See *e.g.* H. Hoberg, D. Schaefer, G. Burkhart, C. Krüger and M. J. Romão, *J. Organomet. Chem.*, 1984, **266**, 203–224; H. Hoberg, Y. Peres, C. Krüger and Y.-H. Tsay, *Angew. Chem., Int. Ed. Engl.*, 1987, **26**, 771–773.